

ADVANCED FUNCTIONAL MATERIALS

Supporting Information

for *Adv. Funct. Mater.*, DOI: 10.1002/adfm.202008306

Atomic Structure and Electron Magnetic Circular
Dichroism of Individual Rock Salt Structure Antiphase
Boundaries in Spinel Ferrites

*Zhuo Li, Jinlian Lu, Lei Jin, Ján Ruzs, Vancho Kocevski,
Hideto Yanagihara, Eiji Kita, Joachim Mayer, Rafal E.
Dunin-Borkowski, Hongjun Xiang,* and Xiaoyan Zhong**

Supporting Information

Atomic Structure and Electron Magnetic Circular Dichroism of Individual Rock Salt Structure Antiphase Boundaries in Spinel Ferrites

Zhuo Li¹, Jinlian Lu¹, Lei Jin, Ján Ruzs, Vancho Kocevski, Hideto Yanagihara, Eiji Kita, Joachim Mayer, Rafal E. Dunin-Borkowski, Hongjun Xiang^{*}, Xiaoyan Zhong^{*}

CONTENT

SUPPORTING FIGURES	2
SUPPORTING TABLE.....	12
SUPPORTING DISCUSSION.....	15
<i>Analysis of SNR and confidence level of EMCD spectra</i>	<i>15</i>
<i>Dynamical diffraction calculations and qualitative analysis of EMCD spectra</i>	<i>20</i>
<i>Statistical analysis and error bars</i>	<i>30</i>
<i>DFT calculation details and the J values of defect-free structure for different unit cell volumes.....</i>	<i>36</i>
<i>Magnetic coupling in the Imma-APB NiFe₂O₄ structure by DFT calculations.....</i>	<i>37</i>
REFERENCES	39

Supporting Figures

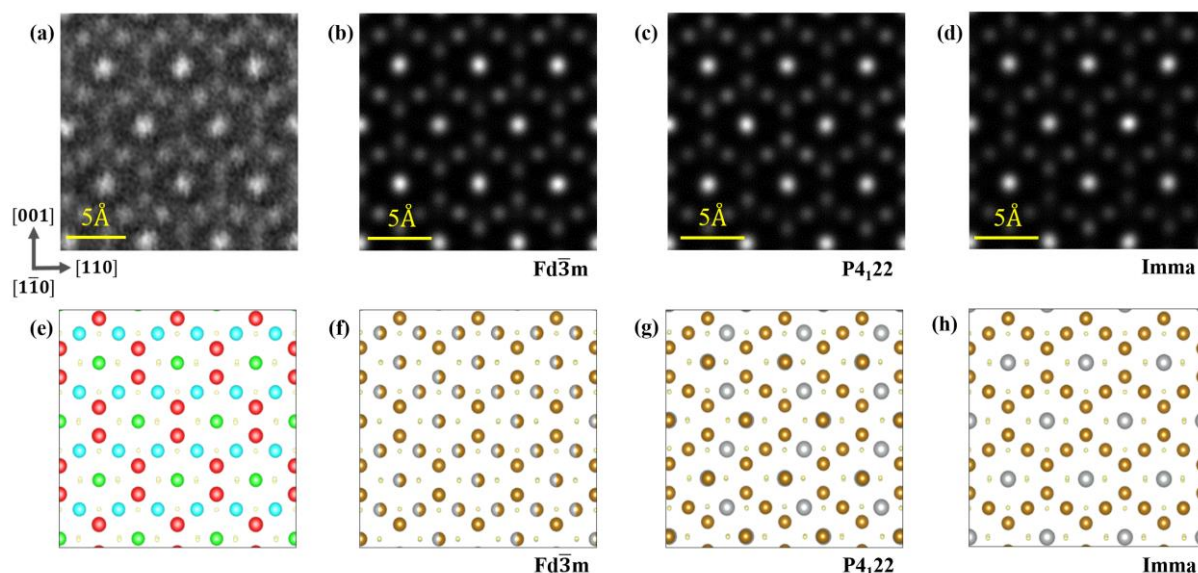


Figure S1. (a) High-angle annular dark-field scanning transmission electron microscopy (HAADF STEM) image of perfectly ordered NiFe_2O_4 viewed in the $[1\bar{1}0]$ direction. (b-d) Simulated HAADF STEM images of perfectly ordered NiFe_2O_4 with (b) $Fd\bar{3}m$, (c) $P4_122$ and (d) $Imma$ symmetries. The images are very similar. (e) Atomic model of perfectly ordered NiFe_2O_4 viewed in the $[1\bar{1}0]$ direction. Atomic columns with metal atoms fully occupying octahedral interstices are shown in green; atomic columns with metal atoms occupying half of the octahedral interstices are shown in blue; atomic columns with Fe atoms occupying tetrahedral interstices are shown in red. (f) Atomic model of perfectly ordered NiFe_2O_4 with $Fd\bar{3}m$ symmetry viewed in the $[1\bar{1}0]$ direction. (g, h) Atomic models of perfectly ordered NiFe_2O_4 viewed in the $[1\bar{1}0]$ direction with (g) $P4_122$ and (h) $Imma$ symmetry relaxed using first-principles density functional theory calculations. In (f), (g) and (h) the Fe, Ni and O ions are shown in gold, silver and yellow, respectively.

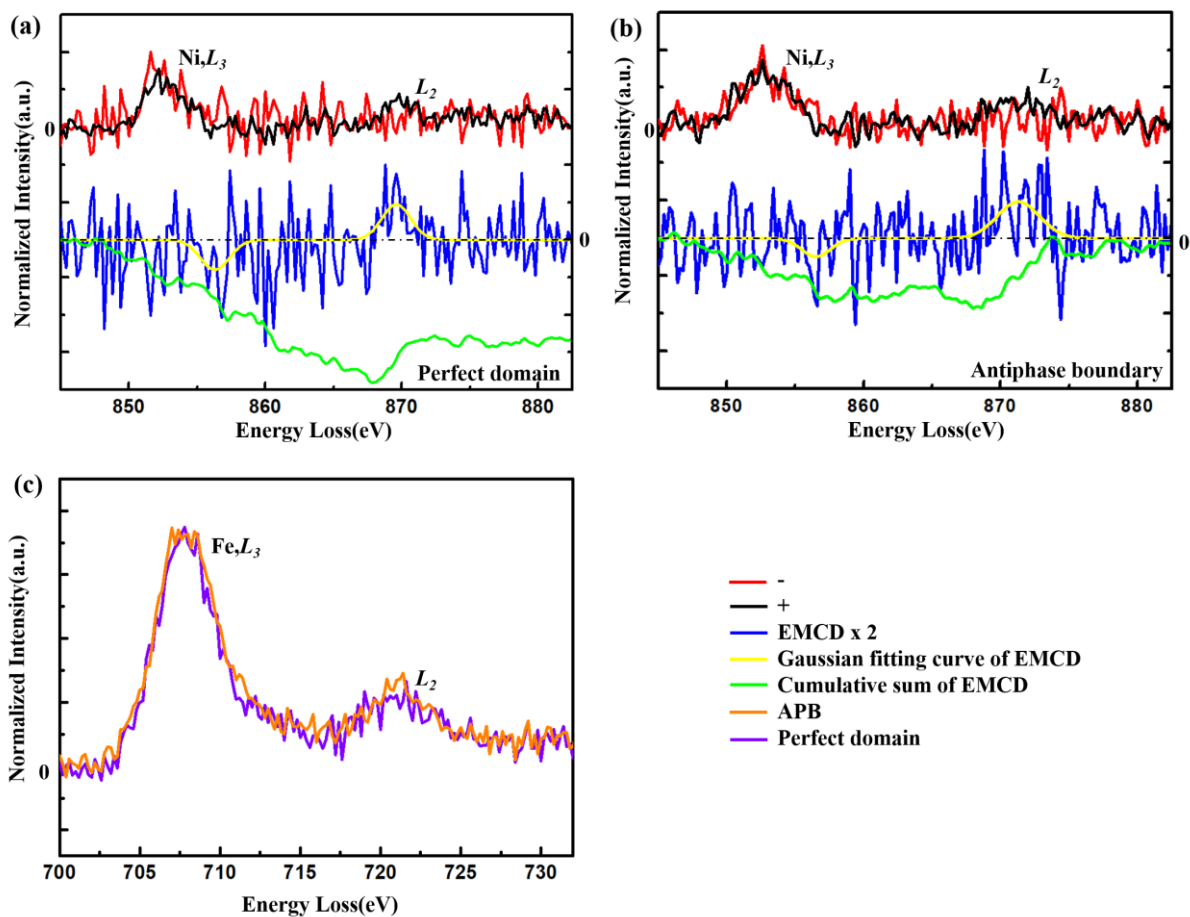


Figure S2. (a) Normalized electron energy-loss (EEL) spectra recorded from positive “+” (black) and negative “-” (red) detector positions, shown alongside electron magnetic circular dichroism (EMCD) spectra (blue), Gaussian curve fitting (yellow) and integration signals (green) for Ni in (a) a perfect NiFe₂O₄ domain and (b) within an antiphase boundary (APB). (c) EEL near-edge fine structures of Fe recorded inside a perfect domain (violet) and within the APB (orange).

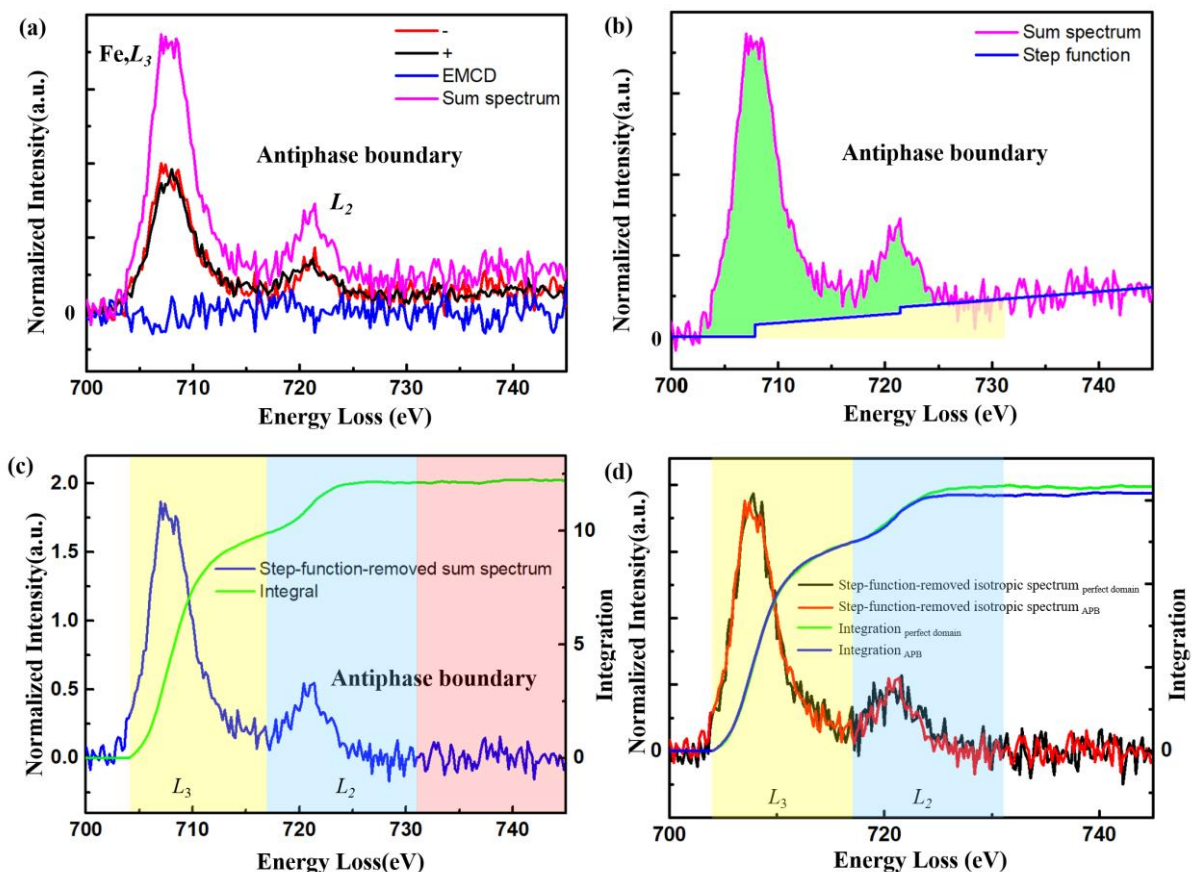


Figure S3. (a) Processed EEL spectra acquired from positive and negative detector positions from the APB with ‘+’ in black and ‘-’ in red, respectively. The difference and sum of the ‘+’ and ‘-’ EEL spectra are marked “EMCD” in blue and “sum spectrum” in purple, respectively. (b) The sum spectrum (purple), with a corresponding step function (blue). The area used for calculating the white-line intensity is filled by a green color, while the area of the step function over the $L_{2,3}$ edges is filled by a yellow color. (c) The step-function-removed sum spectrum (blue) and its intensity integral (green). The post-edge area for error estimation is highlighted by a red color, while the L_3 and L_2 areas are highlighted by yellow and blue colors, respectively. (d) Step-function-removed isotropic spectrum normalized over the L_3 edge for the perfect domain (black) and the APB (red), shown alongside corresponding integration curves for the perfect domain (green) and the APB (blue).

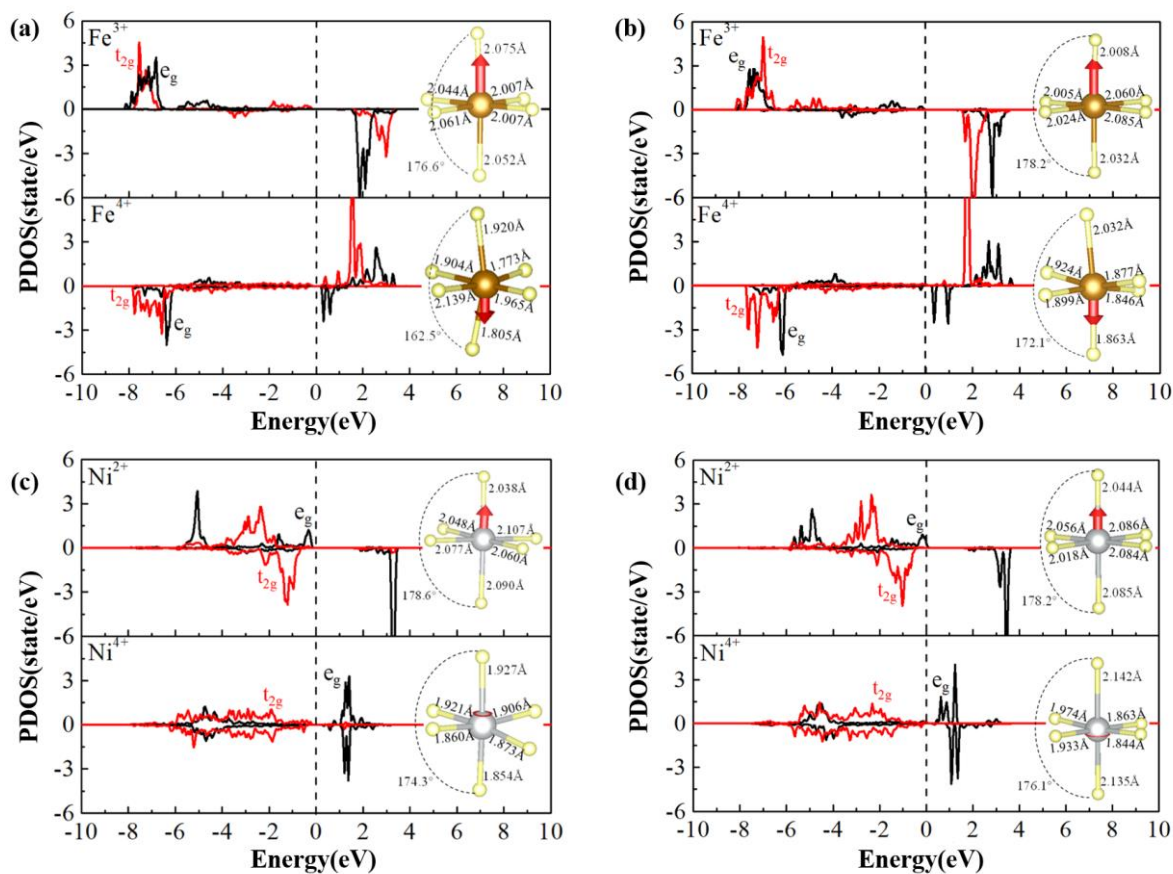


Figure S4. (a) PDOS of Fe³⁺ (upper panel) inside the perfect domain and Fe⁴⁺ (lower panel) within the APB interlayer for the $P4_122 - APB$ structure. The inset shows the angle of O-Fe-O and the bond lengths between Fe and the closest O atoms. (b) As for panel (a), but for the $Imma - APB$ structure. (c) PDOS for Ni²⁺ (upper panel) within the perfect domain and Ni⁴⁺ (lower panel) within the APB interlayer for the $P4_122 - APB$ structure. The inset shows the angle of O-Ni-O and the bond lengths between Ni and the closest O atoms. (d) As for panel (c), but for the $Imma - APB$ structure.

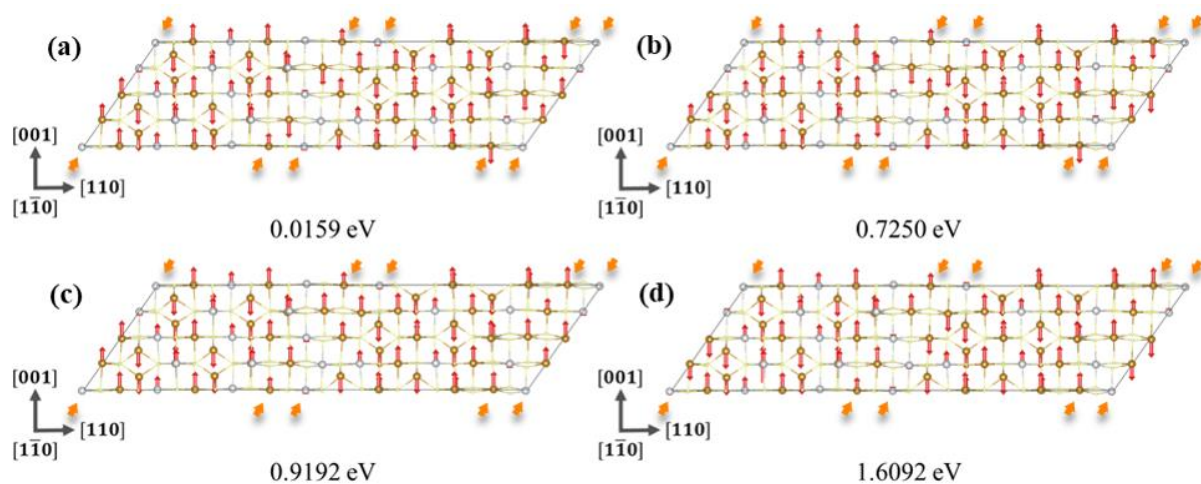


Figure S5. Magnetic structures for the $P4_122 - APB$ model with alternative magnetic ordering of the Fe magnetic moments in rock salt structure interlayers and values of the relative system energy compared to the $P4_122 - APB$ model shown in Figure 4b. Regardless of the calculated exchange parameters in the APB interlayer, random combinations of magnetic interactions within the APB interlayer were laid out for testing. This figure confirms that for the $P4_122 - APB$ model the magnetic structure deduced from the calculated exchange parameters (J) in Figure 4b is the most stable structure, *i.e.*, having the lowest energy.

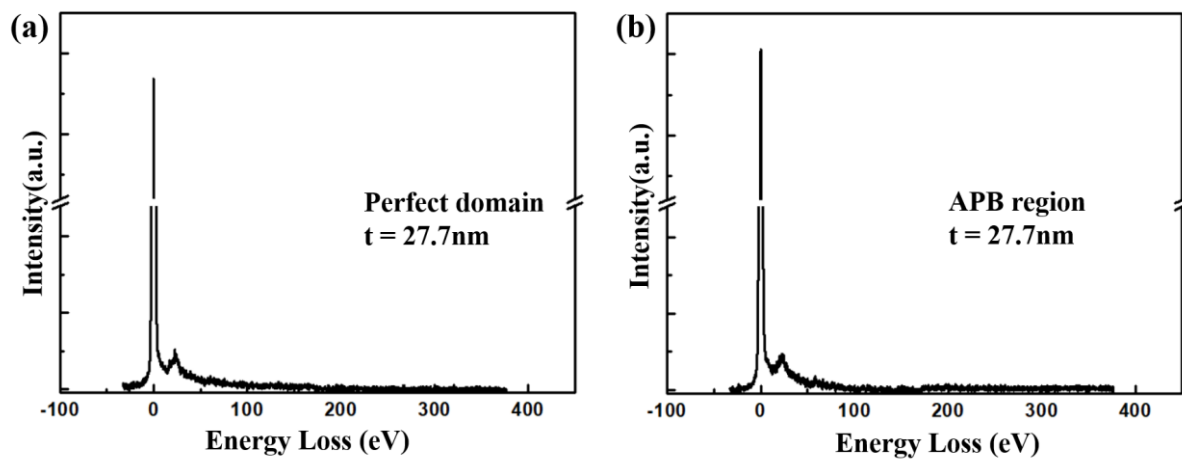


Figure S6. Low-loss electron energy-loss spectra recorded from (a) a perfect domain and (b) the antiphase boundary (APB) region. The inferred specimen thickness is 27.7 nm.

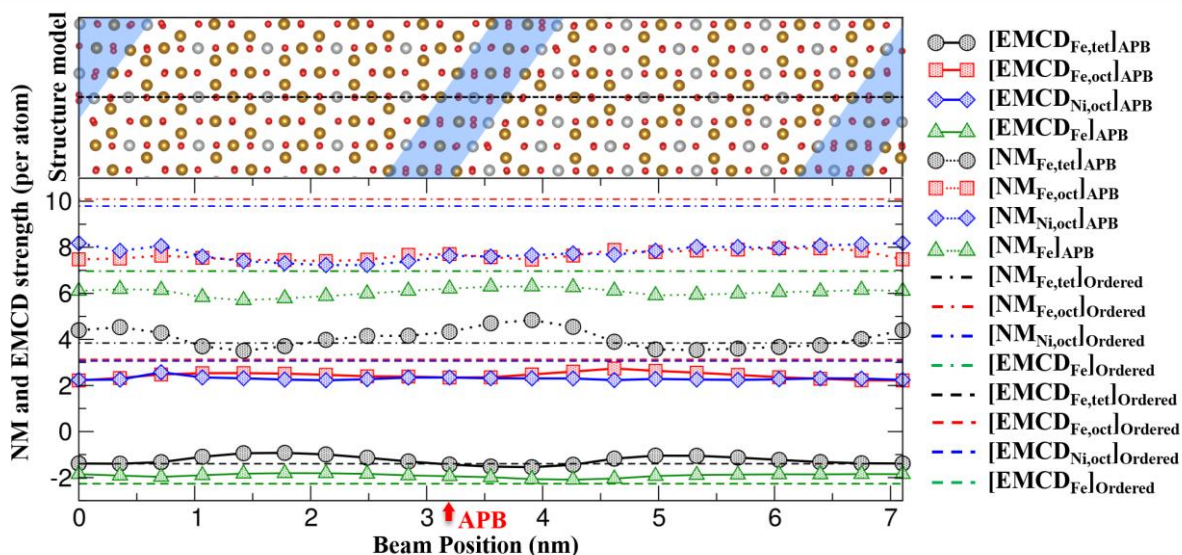


Figure S7. Electron-beam-position-dependent strengths of the calculated dynamical diffraction coefficients of the non-magnetic (NM) part and the magnetic (electron magnetic circular dichroism, EMCD) part evaluated on the assumption that Fe and Ni atoms in the octahedral interstices do not change their electronic structure, magnetic moment direction or strength within the antiphase boundary (APB) interlayer compared to perfectly ordered NiFe_2O_4 . The plots show simulated electron beam scans along the dashed black line in the middle of the $P4_122$ – APB atomic model, with the position of the APB shadowed in blue. Absolute coefficient numbers from the APB region are taken at the position marked by a red arrow on the x axis.

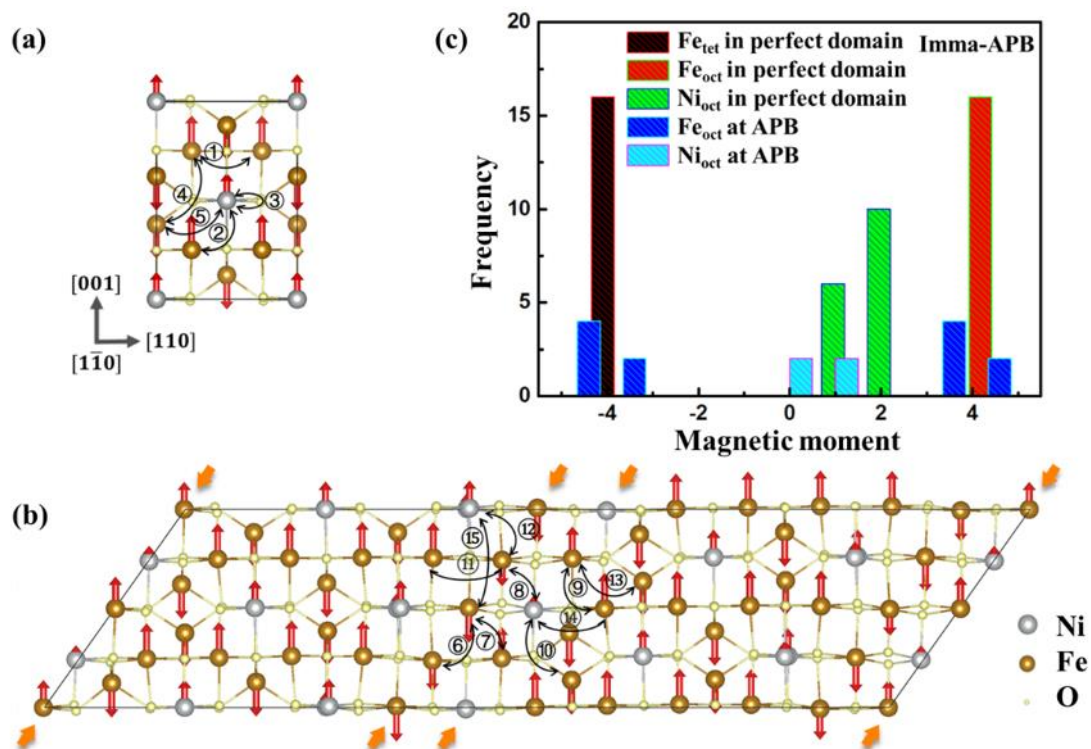


Figure S8. First-principles density functional theory magnetic calculations of NiFe₂O₄ for (a) the *Imma* structure and (b) the *Imma* structure with an antiphase boundary (*Imma* – APB). Atomic interlayers with the rock salt structure are marked with orange arrows. The lengths of the red arrows indicate the magnitudes of the magnetic moments, while the directions of the magnetic moments are determined from calculated exchange parameters (J). The arrow length for Ni is magnified by a factor of two for better visibility. (c) Magnetic moment histograms for atoms in the *Imma* – APB model.

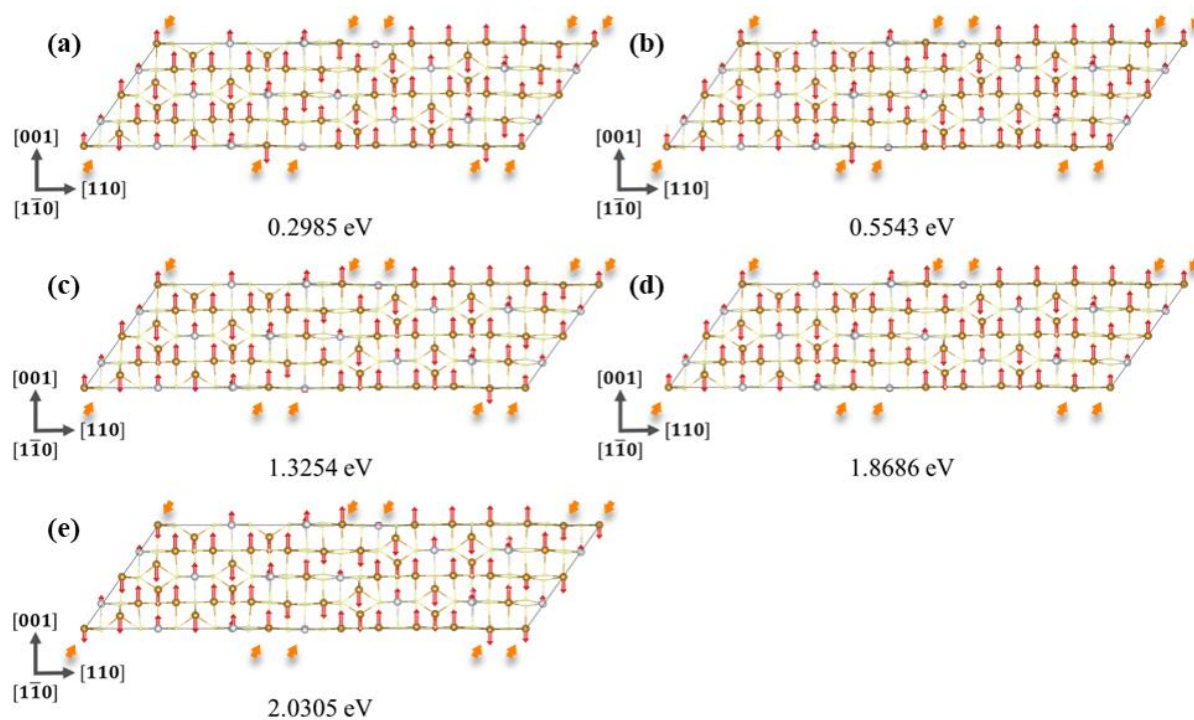


Figure S9. Magnetic structures for the $Imma - APB$ model with different magnetic orders of the Fe magnetic moments within the rock salt structure interlayers and values of relative system energy compared to the $Imma - APB$ model shown in Figure S6b. Atomic interlayers with the rock salt structure are marked with orange arrows. Regardless of the calculated exchange parameters in the APB interlayer, random combinations of magnetic interactions at the APB interlayer were laid out for testing. This figure confirms that, for the $Imma - APB$ model, the magnetic structure deduced from the calculated exchange parameters (J) in Figure S8b is the most stable structure, *i.e.*, having the lowest energy.

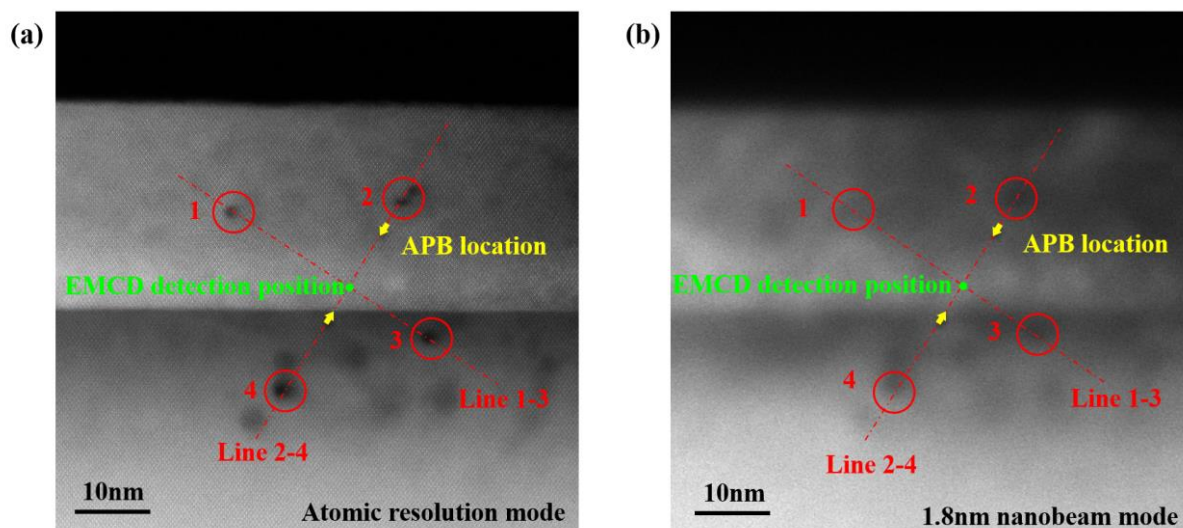


Figure S10. Illustration of tracking the same antiphase boundary (APB) in atomic-resolution and nanobeam scanning transmission electron microscopy (STEM) modes using electron-beam-drilled fiducial markers. (a) High-resolution high-angle annular dark-field STEM image, showing four holes drilled by the electron beam (marked by red circles) viewed in the $[1\bar{1}0]$ direction. The APB is located between the yellow arrows. The position at which an electron magnetic circular dichroism (EMCD) signal was recorded from the APB is marked by a green dot and is located at the intersection of lines 1-3 and 2-4. (b) Image of the same area recorded after switching to nanobeam mode.

Supporting Table

Table S1. Exchange parameters (J) (in eV) for the *Imma* structure with an antiphase boundary (*Imma* – APB).

Imma	Angle	¹⁾ Number	Atom ₁	Atom ₂	J [eV]
order	90°	①	Fe _{oct}	Fe _{oct}	0.0029
		②	Fe _{oct}	Ni _{oct}	-0.0010
		③	Ni _{oct}	Ni _{oct}	-0.0012
	120°	④	Fe _{tet}	Fe _{oct}	0.0343
		⑤	Fe _{tet}	Ni _{oct}	0.0223
APB	90°	⑥	Fe _{oct}	Fe _{oct}	0.0032
		⑦	Fe _{oct}	Fe _{oct}	0.0105
		⑧	Fe _{oct}	Ni _{oct}	0.0120
		⑨	Fe _{oct}	Fe _{oct}	0.0076
		⑩	Fe _{tet}	Ni _{oct}	-0.0100
	120°	⑪	Fe _{oct}	Fe _{oct}	0.0087
		⑫	Fe _{oct}	Ni _{oct}	-0.0126
		⑬	Fe _{tet}	Fe _{oct}	0.0468
		⑭	Fe _{oct}	Ni _{oct}	0.0000
		⑮	Fe _{oct}	Ni _{oct}	0.0277

¹⁾The sequence numbers correspond to those indicated in Figure S8.

Table S2. Exchange parameters (J) (in eV) for the $P4_122$ structure with an antiphase boundary ($P4_122 - APB$).

$P4_122$	Angle	Number	Atom ₁	Atom ₂	J [eV]	
					$U_{Fe} = 4.5$ eV $U_{Ni} = 4.0$ eV	$U_{Fe} = 4.0$ eV $U_{Ni} = 3.0$ eV
Ordered	90°	1	Fe _{oct}	Fe _{oct}	0.0012	0.0015
		2	Fe _{oct}	Ni _{oct}	-0.0014	-0.0017
		3	Ni _{oct}	Ni _{oct}	-0.0012	-0.0014
	120°	4	Fe _{tet}	Fe _{oct}	0.0352	0.0353
		5	Fe _{tet}	Ni _{oct}	0.0178	0.0205
APB	90°	7	Fe _{oct}	Fe _{oct}	0.0326	0.0339
		8	Fe _{oct}	Fe _{oct}	0.0067	0.0076
	120°	10	Fe _{tet}	Fe _{oct}	0.0565	0.0627
	170°	11	Fe _{oct}	Fe _{oct}	0.0339	0.0361
		13	Fe _{oct}	Ni _{oct}	0.0276	0.0220

Table S3. Exchange parameters (J) (in eV) for the ordered $P4_122$ structure.

$P4_122$	Angle	Number	Atom ₁	Atom ₂	J [eV]	
					$V = 2349.78$ Å	$V = 2363.82$ Å
Ordered	90°	1	Fe _{oct}	Fe _{oct}	0.0012	0.0016
		2	Fe _{oct}	Ni _{oct}	-0.0014	-0.0011
		3	Ni _{oct}	Ni _{oct}	-0.0012	-0.0011
	120°	4	Fe _{tet}	Fe _{oct}	0.0352	0.0328
		5	Fe _{tet}	Ni _{oct}	0.0178	0.0176

Supporting discussion

Analysis of SNR and confidence level of EMCD spectra

Based on a previously published criterion ^[13a], the confidence level of an electron magnetic circular dichroism (EMCD) spectrum can be determined by fitting the EMCD signal using the following expression for two Gaussian peaks:

$$f(E) = A_3 e^{-\left(\frac{E-\mu_3}{\sigma_3}\right)^2} + A_2 e^{-\left(\frac{E-\mu_2}{\sigma_2}\right)^2},$$

where E represents an independent variable of energy, μ (in units of eV) represents the centroids of both peaks, μ_3 is constrained to lie between 704 and 717 eV for Fe and between 849 and 861 eV for Ni, μ_2 is constrained to lie between 717 and 731 eV for Fe and between 866 and 878 eV for Ni ^[11a, 39] and σ (in units of eV) is related to the peak width and is constrained to lie between 1.5 and 2.5 eV for both peaks, considering the energy resolution and core hole life time broadening ^[13a, 40]. A_3 and A_2 (dimensionless quantities) are the maximum values of the peaks at the L_3 and L_2 edges, respectively. They reflect the signal strengths of the individual edges. An estimate of the noise was obtained from the standard deviations of the residuals in the pre-edge and post-edge energy ranges for Fe and Ni, in which there are no EMCD signals. The SNR was then defined as the ratio between the signal and the noise estimate. The confidence level ^[41] could be estimated based on the probability distribution of a noisy quantity about its mean value.

For Fe EMCD spectra recorded from the ordered domain, the parameters were as follows:

Coefficients (with 95% confidence bounds):

$$\mu_3 = 708.1 \text{ eV}$$

$$\mu_2 = 718.2 \text{ eV}$$

$$A_3 = -0.1971$$

$$A_2 = 0.0347$$

$$\sigma_3 = 1.5 \text{ eV}$$

$$\sigma_2 = 1.5 \text{ eV}$$

Root mean square error: 0.0927 eV.

Noise estimation: 0.0912 eV.

SNR on the L_3 edge: $0.1971/0.0912 = 2.16$ (96.92%).

SNR on the L_2 edge: $0.0347/0.0912 = 0.38$ (29.60%).

The Gaussian fitting curve for the Fe EMCD spectra is shown in yellow in Figure 3a.

For Fe spectra recorded from the antiphase boundary (APB), the parameters were as follows:

Coefficients (with 95% confidence bounds):

$$\mu_3 = 706.6 \text{ eV}$$

$$\mu_2 = 718.4 \text{ eV}$$

$$A_3 = -0.1017$$

$$A_2 = 0.0917$$

$$\sigma_3 = 1.5 \text{ eV}$$

$$\sigma_2 = 1.601 \text{ eV}$$

Root mean square error: 0.0591 eV.

Noise estimation: 0.0609 eV.

SNR on the L_3 edge: $0.1017/0.0609 = 1.67$ (90.50%).

SNR on the L_2 edge: $0.0917/0.0609 = 1.50$ (86.64%).

The Gaussian fitting curve for the Fe EMCD spectra is shown in yellow in Figure 3b.

For Ni EMCD spectra recorded from the ordered domain, the parameters were as follows:

Coefficients (with 95% confidence bounds):

$$\mu_3 = 856.3 \text{ eV}$$

$$\mu_2 = 869.6 \text{ eV}$$

$$A_3 = -0.1991$$

$$A_2 = 0.2363$$

$$\sigma_3 = 1.5 \text{ eV}$$

$$\sigma_2 = 1.5 \text{ eV}$$

Root mean square error: 0.2070 eV.

Noise estimation: 0.1875 eV.

SNR on the L_3 edge: $0.1991/0.1875 = 1.06$ (71.08%).

SNR on the L_2 edge: $0.2363/0.1875 = 1.26$ (79.24%).

The Gaussian fitting curve for the Ni EMCD spectra is shown in yellow in Figure S2a.

For Ni spectra recorded at the APB, the parameters were as follows:

Coefficients (with 95% confidence bounds):

$$\mu_3 = 856.5 \text{ eV}$$

$$\mu_2 = 871.3 \text{ eV}$$

$$A_3 = -0.1220$$

$$A_2 = 0.2421$$

$$\sigma_3 = 1.5 \text{ eV}$$

$$\sigma_2 = 2.184 \text{ eV}$$

Root mean square error: 0.1953 eV.

Noise estimation: 0.1556 eV.

SNR on the L_3 edge: $0.1220/0.1556 = 0.78$ (56.46%).

SNR on the L_2 edge: $0.2421/0.1556 = 1.56$ (88.12%).

The Gaussian fitting curve for the Ni EMCD spectra is shown in yellow in Figure S2b.

Given that the fitted value of σ was obtained at the lower bound in some cases, a systematic comparison was performed for different fitting ranges of σ . The resulting SNR and confidence levels for Fe EMCD fitting parameters did not change significantly. For Ni, although the

EMCD data have a lower signal to noise ratio and the confidence level changes are larger in some cases, they do not influence the overall picture. The relatively high root mean square error for Ni originates from the low SNR in the original Ni spectra.

Dynamical diffraction calculations and qualitative analysis of EMCD spectra

Theoretically, an EMCD spectrum can be described in terms of a sum of the EMCD signals from all contributing atoms. The Fe and Ni atoms in perfect NiFe₂O₄, which has an inverse spinel structure, can be grouped into three categories: Fe_{tet}, Fe_{oct} and Ni_{oct}, which represent Fe ions in tetrahedral interstices, and Fe and Ni ions in octahedral interstices, respectively. On the assumption that Fe and Ni atoms in octahedral interstices in the APB do not change their electronic structures or the directions and strengths of their magnetic moments compared to those of Fe and Ni atoms in octahedral interstices in perfectly-ordered NiFe₂O₄, the octahedral sites in the APB could be grouped into the same categories as Fe_{oct} and Ni_{oct} in the perfect domains. By making use of this assumption, it is possible to predict the normalized strengths of EMCD spectra by performing dynamic diffraction calculations of the EMCD coefficients of all of the atoms in the probed area, based on the following derivation method.

Experimental spectra recorded at positive “+” and negative “-” positions under two beam conditions can be expressed as follows.

For Fe:

$$\begin{aligned}
 S_{Fe\pm} = & \{W_{Fe,oct}NM_{Fe,oct}[\mu_+(E) + \mu_-(E) + \mu_0(E)]_{Fe,oct} \\
 & + W_{Fe,tet}NM_{Fe,tet}[\mu_+(E) + \mu_-(E) + \mu_0(E)]_{Fe,tet}\} \\
 & \pm \{W_{Fe,oct}EMCD_{Fe,oct}[\mu_+(E) - \mu_-(E)]_{Fe,oct} \\
 & + W_{Fe,tet}EMCD_{Fe,tet}[\mu_+(E) - \mu_-(E)]_{Fe,tet}\}
 \end{aligned}$$

(S-1)

For Ni:

$$S_{Ni\pm} = NM_{Ni,oct}[\mu_+(E) + \mu_-(E) + \mu_0(E)]_{Ni,oct} \pm EMCD_{Ni,oct}[\mu_+(E) - \mu_-(E)]_{Ni,oct}$$

(S-2)

$$W_{Fe,oct} + W_{Fe,tet} = 1$$

(S-3)

$W_{Fe,oct}$ and $W_{Fe,tet}$ are weighting factors, based on the number of atoms in octahedral and tetrahedral sites, respectively, in the probed area. $[\mu_+(E) - \mu_-(E)]_{Fe,oct}$, $[\mu_+(E) - \mu_-(E)]_{Ni,oct}$ and $[\mu_+(E) - \mu_-(E)]_{Fe,tet}$ describe the intrinsic magnetic circular dichroism (MCD) of Fe_{oct} , Ni_{oct} and Fe_{tet} , respectively. $[\mu_+(E) + \mu_-(E) + \mu_0(E)]_{Fe,oct}$, $[\mu_+(E) + \mu_-(E) + \mu_0(E)]_{Ni,oct}$ and $[\mu_+(E) + \mu_-(E) + \mu_0(E)]_{Fe,tet}$ are intrinsic non-magnetic isotropic spectra from Fe_{oct} , Ni_{oct} and Fe_{tet} , respectively. $EMCD_{Fe,oct}$, $EMCD_{Fe,tet}$ and $EMCD_{Ni,oct}$ are the magnetic parts of the dynamical diffraction coefficients for Fe_{oct} , Fe_{tet} and Ni_{oct} respectively, while $NM_{Fe,oct}$, $NM_{Fe,tet}$ and $NM_{Ni,oct}$ are the non-magnetic parts of the dynamical diffraction coefficients for Fe_{oct} , Fe_{tet} and Ni_{oct} , respectively. They can be determined by using dynamical diffraction calculations for the experimental diffraction conditions, including the convergence semi-angle, collection semi-angle, diffraction geometry and specimen thickness. The specimen thickness of the APB region and the perfect crystal was measured to be 27.7 nm from low-loss electron energy-loss spectra (Figure S6), which is within the optimal thickness range for EMCD detection for the present experimental conditions according to thickness-dependent relative EMCD strengths evaluated by dynamical diffraction calculations^[11a]. The calculated electron-beam-position-dependent strengths per atom of $NM_{Fe,tet}$ (dotted lines in black), $NM_{Fe,oct}$ (dotted lines in red), $NM_{Ni,oct}$ (dotted lines in blue), NM_{Fe} (dotted lines in green), $EMCD_{Fe,tet}$ (solid lines in black), $EMCD_{Fe,oct}$ (solid lines in red), $EMCD_{Ni,oct}$ (solid lines in blue) and $EMCD_{Fe}$ (solid lines in green) across the APB are shown in Figure S7, alongside EMCD (straight dashed lines) and NM (straight dashed-dotted lines) strengths for perfectly-ordered $NiFe_2O_4$ ^[38].

The experimental isotropic spectra can be expressed as follows.

For Fe:

$$(S_+ + S_-)_{Fe} = 2W_{Fe,oct}NM_{Fe,oct}[\mu_+(E) + \mu_-(E) + \mu_0(E)]_{Fe,oct} \\ + 2W_{Fe,tet}NM_{Fe,tet}[\mu_+(E) + \mu_-(E) + \mu_0(E)]_{Fe,tet}$$

(S-4)

For Ni:

$$(S_+ + S_-)_{Ni} = 2NM_{Ni,oct}[\mu_+(E) + \mu_-(E) + \mu_0(E)]_{Ni,oct}$$

(S-5)

The experimental EMCD spectra can be expressed as follows.

For Fe:

$$(S_+ - S_-)_{Fe} = 2W_{Fe,oct}EMCD_{Fe,oct}[\mu_+(E) - \mu_-(E)]_{Fe,oct} \\ + 2W_{Fe,tet}EMCD_{Fe,tet}[\mu_+(E) - \mu_-(E)]_{Fe,tet}$$

(S-6)

For Ni:

$$(S_+ - S_-)_{Ni} = 2EMCD_{Ni,oct}[\mu_+(E) - \mu_-(E)]_{Ni,oct}$$

(S-7)

Based on the previous assumption, the magnetic moments of Fe and Ni in the APB model are almost unchanged in comparison with the calculated magnetic moments of Fe and Ni in

perfectly-ordered NiFe_2O_4 . Considering antiferromagnetic coupling between Fe_{oct} and Fe_{tet} , the following approximation can be made for simplicity:

$$\begin{aligned} [\mu_+(E) + \mu_-(E) + \mu_0(E)]_{\text{Fe}} &= [\mu_+(E) + \mu_-(E) + \mu_0(E)]_{\text{Fe,oct}} \\ &\approx [\mu_+(E) + \mu_-(E) + \mu_0(E)]_{\text{Fe,tet}} \end{aligned}$$

(S-8)

$$[\mu_+(E) - \mu_-(E)]_{\text{Fe}} = [\mu_+(E) - \mu_-(E)]_{\text{Fe,oct}} \approx -[\mu_+(E) - \mu_-(E)]_{\text{Fe,tet}}$$

(S-9)

$(S_+ + S_-)_{\text{Fe}}$ and $(S_+ - S_-)_{\text{Fe}}$ can then be simplified as follows:

$$(S_+ + S_-)_{\text{Fe}} = 2(W_{\text{Fe,oct}}NM_{\text{Fe,oct}} + W_{\text{Fe,tet}}NM_{\text{Fe,tet}})[\mu_+(E) + \mu_-(E) + \mu_0(E)]_{\text{Fe}}$$

(S-10)

$$(S_+ - S_-)_{\text{Fe}} = 2(W_{\text{Fe,oct}}EMCD_{\text{Fe,oct}} - W_{\text{Fe,tet}}EMCD_{\text{Fe,tet}})[\mu_+(E) - \mu_-(E)]_{\text{Fe}}$$

(S-11)

For Fe:

$$\begin{aligned} \int_{L_2} (S_+ - S_-)_{\text{Fe}} dE \\ = 2(W_{\text{Fe,oct}}EMCD_{\text{Fe,oct}} - W_{\text{Fe,tet}}EMCD_{\text{Fe,tet}}) \int_{L_2} [\mu_+(E) - \mu_-(E)]_{\text{Fe}} dE \end{aligned}$$

(S-12)

$$\int_{L_3} (S_+ - S_-)_{Fe} dE$$

$$= 2(W_{Fe,oct}EMCD_{Fe,oct} - W_{Fe,tet}EMCD_{Fe,tet}) \int_{L_3} [\mu_+(E) - \mu_-(E)]_{Fe} dE$$

(S-13)

$$\int_{L_{2,3}} (S_+ + S_-)_{Fe} dE$$

$$= 2(W_{Fe,oct}NM_{Fe,oct} + W_{Fe,tet}NM_{Fe,tet}) \int_{L_{2,3}} [\mu_+(E) + \mu_-(E) + \mu_0(E)]_{Fe} dE$$

(S-14)

For Ni:

$$\int_{L_2} (S_+ - S_-)_{Ni} dE = 2EMCD_{Ni,oct} \int_{L_2} [\mu_+(E) - \mu_-(E)]_{Ni,oct} dE$$

(S-15)

$$\int_{L_3} (S_+ - S_-)_{Ni} dE = 2EMCD_{Ni,oct} \int_{L_3} [\mu_+(E) - \mu_-(E)]_{Ni,oct} dE$$

(S-16)

$$\int_{L_{2,3}} (S_+ + S_-)_{Ni} dE = 2NM_{Ni,oct} \int_{L_{2,3}} [\mu_+(E) + \mu_-(E) + \mu_0(E)]_{Ni,oct} dE$$

(S-17)

We applied the following sum rules^[42]:

$$\frac{\int_{L_3} (\mu_+(E) - \mu_-(E))dE + \int_{L_2} (\mu_+(E) - \mu_-(E))dE}{\int_{L_{2,3}} (\mu_+(E) + \mu_-(E) + \mu_0(E))dE} = \frac{\langle L_z \rangle}{2N_h}$$

(S-18)

$$\frac{\int_{L_3} (\mu_+(E) - \mu_-(E))dE - 2 \int_{L_2} (\mu_+(E) - \mu_-(E))dE}{\int_{L_{2,3}} (\mu_+(E) + \mu_-(E) + \mu_0(E))dE} = \frac{2\langle S_z \rangle}{3N_h} + \frac{7\langle T_z \rangle}{3N_h}$$

(S-19)

where $\langle S_z \rangle$, $\langle L_z \rangle$ and $\langle T_z \rangle$ are the ground-state expectation values of the spin momentum, orbital momentum and magnetic dipole operators, respectively. The contribution of the magnetic dipole operators $\langle T_z \rangle$ can usually be ignored in cubic systems. N_h is the number of holes in the 3d orbital.

According to S-18 and S-19, the total magnetic moment $\langle \mu \rangle$ expressed according to sum rules is:

$$\begin{aligned} \langle \mu \rangle &= -\mu_B (\langle L_z \rangle + 2\langle S_z \rangle) \\ &= -\mu_B \cdot N_h \cdot \frac{5 \int_{L_3} (\mu_+(E) - \mu_-(E))dE - 4 \int_{L_2} (\mu_+(E) - \mu_-(E))dE}{\int_{L_{2,3}} (\mu_+(E) + \mu_-(E) + \mu_0(E))dE} \end{aligned}$$

(S-20)

$$\frac{5 \int_{L_3} (\mu_+(E) - \mu_-(E))dE - 4 \int_{L_2} (\mu_+(E) - \mu_-(E))dE}{\int_{L_{2,3}} (\mu_+(E) + \mu_-(E) + \mu_0(E))dE} = \frac{\langle \mu \rangle}{-\mu_B \cdot N_h}$$

(S-21)

By making use of Equations S-12, S-13 and S-14, Equation S-21 can be rewritten for Fe in the following way:

$$\frac{5 \int_{L_3} (S_+ - S_-)_{Fe} dE - 4 \int_{L_2} (S_+ - S_-)_{Fe} dE}{\int_{L_{2,3}} (S_+ + S_-)_{Fe} dE} = \frac{\langle \mu \rangle_{Fe}}{-\mu_B \cdot N_{h,Fe}} \cdot \frac{W_{Fe,oct} EMCD_{Fe,oct} - W_{Fe,tet} EMCD_{Fe,tet}}{W_{Fe,oct} NM_{Fe,oct} + W_{Fe,tet} NM_{Fe,tet}}$$

(S-22)

By making use of Equations S-15, S-16 and S-17, Equation S-21 can be rewritten for Ni in the following way:

$$\frac{5 \int_{L_3} (S_+ - S_-)_{Ni} dE - 4 \int_{L_2} (S_+ - S_-)_{Ni} dE}{\int_{L_{2,3}} (S_+ + S_-)_{Ni} dE} = \frac{\langle \mu \rangle_{Ni}}{-\mu_B \cdot N_{h,Ni}} \cdot \frac{EMCD_{Ni,oct}}{NM_{Ni,oct}}$$

(S-23)

The normalized strength of EMCD spectra is defined as

$$NS_{emcd} = \frac{5 \int_{L_3} (S_+ - S_-) dE - 4 \int_{L_2} (S_+ - S_-) dE}{\int_{L_{2,3}} (S_+ + S_-) dE} = 5 \int_{L_3} (S_+ - S_-)_N dE - 4 \int_{L_2} (S_+ - S_-)_N dE$$

(S-24)

where $\int_{L_3} (S_+ - S_-)_N dE$ and $\int_{L_2} (S_+ - S_-)_N dE$ are integrals over normalized EMCD spectra at the L_3 and L_2 edges, respectively.

The normalized strength of EMCD spectra for Fe is

$$\begin{aligned} NS_{emcd,Fe} &= 5 \int_{L_3} (S_+ - S_-)_{N_{Fe}} dE - 4 \int_{L_2} (S_+ - S_-)_{N_{Fe}} dE \\ &= \frac{\langle \mu \rangle_{Fe}}{-\mu_B \cdot N_{h,Fe}} \cdot \frac{W_{Fe,oct} EMCD_{Fe,oct} - W_{Fe,tet} EMCD_{Fe,tet}}{W_{Fe,oct} NM_{Fe,oct} + W_{Fe,tet} NM_{Fe,tet}}. \end{aligned}$$

(S-25)

The normalized strength of EMCD spectra for Ni is

$$NS_{emcd,Ni} = 5 \int_{L_3} (S_+ - S_-)_{N_{Ni}} dE - 4 \int_{L_2} (S_+ - S_-)_{N_{Ni}} dE = \frac{\langle \mu \rangle_{Ni}}{-\mu_B \cdot N_{h,Ni}} \cdot \frac{EMCD_{Ni,oct}}{NM_{Ni,oct}}$$

(S-26)

These quantities can be calculated from normalized EMCD spectra from the APB region and the perfect domain, as shown in Figures 3a and 3b for Fe and Figure S2a and Figure S2b for Ni.

The relative EMCD strength coefficient for Fe is defined as (Figure 3c)

$$REMCD_{Fe} = \frac{-W_{Fe,oct} EMCD_{Fe,oct} + W_{Fe,tet} EMCD_{Fe,tet}}{4(W_{Fe,oct} NM_{Fe,oct} + W_{Fe,tet} NM_{Fe,tet})}.$$

(S-27)

The relative EMCD strength coefficient for Ni is defined as (Figure 3c)

$$REMCD_{Ni} = \frac{EMCD_{Ni,oct}}{2NM_{Ni,oct}}.$$

(S-28)

On the assumption that Fe and Ni atoms in octahedral interstices in the APB do not change their electronic structure, or their magnetic moment directions or strengths, when compared to Fe and Ni atoms in octahedral interstices in perfectly-ordered $NiFe_2O_4$, $\langle\mu\rangle_{Fe}$, $\langle\mu\rangle_{Ni}$, $N_{h,Fe}$ and $N_{h,Ni}$ appear to remain unchanged at the APB, when compared to the perfect domains, resulting in the same values of $\frac{\langle\mu\rangle_{Fe}}{-\mu_B \cdot N_{h,Fe}}$ and $\frac{\langle\mu\rangle_{Ni}}{-\mu_B \cdot N_{h,Ni}}$ at the APB as in the perfect domains.

The normalized strength of the EMCD spectra NS_{emcd} is then proportional to the REMCD. The strengths of $NM_{Fe,tet}$, $EMCD_{Fe,tet}$, $NM_{Fe,oct}$ and $EMCD_{Fe,oct}$ for the perfectly-ordered model are 3.844, -1.399, 10.090 and 3.134, respectively. Ideally, the ratio of the number of Fe_{oct} to Fe_{tet} remains 1:1 for perfectly-ordered $NiFe_2O_4$ with an inverse spinel structure, indicating that $W_{Fe,oct} = W_{Fe,tet} = 0.5$. The strength of $REMCD_{Fe}$ in perfectly-ordered $NiFe_2O_4$, which is indicated by a dashed green line in Figure 3c, is calculated to be -8.4%. The strengths of $NM_{Fe,tet}$, $EMCD_{Fe,tet}$, $NM_{Fe,oct}$ and $EMCD_{Fe,oct}$ within the APB region are 4.330, -1.435, 7.704, and 2.346, respectively. It should be noted that the number of atoms occupying tetrahedral sites near the APB is lower than that in the perfectly-ordered regions as a result of the presence of the rock salt structure interlayer with only octahedral sites. The percentage of atoms occupying tetrahedral sites is reduced as the beam approaches the APB. $W_{Fe,oct}$ and $W_{Fe,tet}$ can be determined from the probe size and position when scanning across the APB. The strength of $REMCD_{Fe}$ at the APB is calculated to be -7.9%. The strengths of $NM_{Ni,oct}$ and $EMCD_{Ni,oct}$ for the perfectly-ordered model are 9.790 and 3.063, respectively. The strength of $REMCD_{Ni}$ in perfectly-ordered $NiFe_2O_4$ is calculated to be 7.8%. The

strengths of $NM_{Ni,oct}$ and $EMCD_{Ni,oct}$ at the APB position are 7.632 and 2.347, respectively. The strength of $REMCD_{Ni}$ at the APB is calculated to be 7.7%. Electron-beam-position-dependent dynamical diffraction calculations show that the strengths of $REMCD_{Fe}$ and $REMCD_{Ni}$ are approximately constant across the APB and are close to those calculated for perfectly-ordered $NiFe_2O_4$. Considering that the normalized strengths of the EMCD spectra NS_{emcd} are proportional to the REMCD, NS_{emcd} for Fe and Ni are also predicted to be approximately constant across the APB, close to those calculated from perfectly-ordered $NiFe_2O_4$ based on the current assumption.

By using the experimental EMCD Fe and Ni spectra recorded in the APB region and the perfect domains, as shown in Figures 3 and S2, the experimental integrals $\int_{L_3} (S_+ - S_-)_N dE$ and $\int_{L_2} (S_+ - S_-)_N dE$ over the normalized EMCD spectra can be obtained at the L_3 and L_2 edges, respectively. The strengths of NS_{emcd} for Fe inside the perfect domains and within the APB are -0.26 ± 0.04 and -0.14 ± 0.01 , respectively. The strengths of NS_{emcd} for Ni in the perfect domains and within the APB are -0.91 ± 0.14 and -0.56 ± 0.10 , respectively. Thus, there is a $46.8\% \pm 8.2\%$ and approximately a $38.8\% \pm 14.5\%$ reduction in the normalized strengths of the EMCD spectra (NS_{emcd}) for Fe and Ni, respectively, at the APB when compared to the perfect domains.

There is a contradiction between the experimental and theoretically-predicted results, with regard to the normalized strengths of the EMCD spectra. The assumption in the theoretical calculation is therefore inferred to be incorrect, indicating that the atoms at the APB have different electronic structures, with different magnitudes and/or directions of their magnetic moments.

Statistical analysis and error bars

In this section, we present in detail the procedures for error estimation and explain how the error bar for NS_{emcd} ($S_{NS_{emcd}}$) and the error bar for the relative reduction of NS_{emcd} between the APB and the perfect domain are calculated. According to Equation (S-24), we estimate the error bar for NS_{emcd} by calculating the individual error bars for the integrals of $\int_{L_{2,3}} (S_+ + S_-) dE$ and $5 \int_{L_3} (S_+ - S_-) dE - 4 \int_{L_2} (S_+ - S_-) dE$.

a) Error estimation of $\int_{L_{2,3}} (S_+ + S_-) dE$

The term $\int_{L_{2,3}} (S_+ + S_-) dE$ in the denominator of Equation (S-24) represents the white line intensity of the isotropic spectra. For the Fe L edges acquired from the APB, Figure S3 shows the procedure to obtain the step-function-removed sum spectrum and to calculate the white line intensity from it.

The raw '+' and '-' EEL spectra recorded from positive and negative detector positions were first background-subtracted using a power-law function, deconvolved by low-loss spectra using a Fourier-ratio method to remove multiple scattering effects and normalized using post-edge regions. The processed EEL spectra recorded from positive and negative positions from the APB are shown as '+' in black and '-' in red in Figure S3a, respectively. The difference (EMCD) and sum of the '+' and '-' EEL spectra are indicated by blue and purple colors, respectively. The sum spectrum reveals isotropic Fe EEL spectra, which can be used for quantitative calculations of white line intensities.

The next step is to remove step functions from the sum spectra. Following standard procedures to determine the shape of the step function,^[31] a straight line was fitted to the post-

edge energy range following the L_2 peak and extrapolated into the L_2 and L_3 region. This line was modified into a double step of the same slope with onsets at the maxima of the spectral peaks. The ratio of the step heights was chosen to be 2:1, in accordance with the multiplicity of the initial states (four $2p_{3/2}$ electrons vs two $2p_{1/2}$ electrons, respectively). By subtracting the step functions from the corresponding sum spectra, the area marked by a green color can be used to calculate the white-line intensity, while the area of the step functions under the $L_{2,3}$ edges is highlighted in yellow, as shown in Figure S3b. Figure S3c shows the step-function-removed sum spectrum and its intensity integral. The white line intensity over the $L_{2,3}$ edges, for which we obtained a value of 12.14, is the intensity integral from 707.8eV to 731eV in the step-function-removed sum spectra recorded from the APB region.

The blue curve in Figure S3c shows that intensities above 731 eV in the post-edge region of the step-function-removed sum spectra are fluctuating around the zero value. These fluctuations are attributed primarily to experimental noise. In order to estimate the errors in the Fe white line intensities due to experimental noise, we performed a statistical analysis of the integral values, including the 71 intensity data points between 731 and 745 eV, as shown by the green curve in Figure S3c. We also performed a similar statistical analysis of the integral values, including 71 intensity data points between 878 and 892 eV for the Ni white line intensities. The values and corresponding standard deviations S_{WL} of the Fe and Ni white line intensities $\int_{L_{2,3}} (S_+ + S_-) dE$ in units of eV are as follows:

For Fe

Inside the perfect domain: 10.886 ± 0.037

Within the APB: 12.139 ± 0.052

For Ni:

Inside the perfect domain: 8.623 ± 0.233

In the APB: 7.847 ± 0.262

b) Error estimation of $5 \int_{L_3} (S_+ - S_-) dE - 4 \int_{L_2} (S_+ - S_-) dE$:

$\int_{L_3} (S_+ - S_-) dE$ and $\int_{L_2} (S_+ - S_-) dE$ represent integrals of the EMCD spectrum over the L_3 and L_2 edges, respectively. Normally, the integrals of $\int_{L_3} (S_+ - S_-) dE$ and $\int_{L_2} (S_+ - S_-) dE$ are negative and positive, respectively. Therefore, the absolute signal value of $5 \int_{L_3} (S_+ - S_-) dE - 4 \int_{L_2} (S_+ - S_-) dE$ is larger than the absolute signal value of $5 \int_{L_3} (S_+ - S_-) dE + 5 \int_{L_2} (S_+ - S_-) dE$, which is $5 \int_{L_{3,2}} (S_+ - S_-) dE$. Considering that a lower signal strength leads to a reduced signal to noise ratio, here we use the standard deviation of $5 \int_{L_{3,2}} (S_+ - S_-) dE$ to conservatively estimate the standard deviation of $5 \int_{L_3} (S_+ - S_-) dE - 4 \int_{L_2} (S_+ - S_-) dE$ in our error analysis.

As shown in Figure 3 and Figure S2, the EMCD spectra for Fe and Ni in the post-edge region fluctuate around zero. This is attributed primarily to experimental noise, since there is no expected EMCD signal in the post-edge energy region. In order to estimate the errors in the integral $\int_{L_{3,2}} (S_+ - S_-) dE$ from the experimental noise, we performed a statistical analysis of the integral values, including 96 intensity data points between energies of 731 and 750 eV in Fe EMCD spectra recorded from the perfect domains and integral values including 30 intensity data points between energies of 731 and 736.8 eV in Fe EMCD spectra recorded from the APB region. Similarly, we performed a statistical analysis of the integral values, including 106 intensity data points between energies of 878 and 899 eV, for Ni EMCD spectra. The standard deviations of the integral $5 \int_{L_{3,2}} (S_+ - S_-) dE$ for the Fe EMCD spectra

recorded from the perfect domain and the APB region are 0.159 and 0.120, respectively, while the standard deviations of the integral $5 \int_{L_{3,2}} (S_+ - S_-) dE$ for the Ni EMCD spectra recorded from the perfect domain and the APB region are 1.148 and 0.789, respectively.

The value and error of $5 \int_{L_3} (S_+ - S_-) dE - 4 \int_{L_2} (S_+ - S_-) dE$ can be summarized as follows:

For Fe:

In the perfect domain: -2.620 ± 0.159

In the APB: -1.700 ± 0.120

For Ni:

In the perfect domain: -7.831 ± 1.148

In the APB: -4.366 ± 0.789

We also considered an independent dataset of Fe L edges recorded from the perfect domain in STEM mode with an exposure time of 15 s, and we have carefully confirmed that the diffraction condition was the same as for the experimental data discussed in the previous sections and the main text. By using new spectra recorded from the perfect domain for Fe, $\int_{L_{2,3}} (S_+ + S_-) dE$ is determined to be 11.664 ± 0.045 , while $5 \int_{L_3} (S_+ - S_-) dE - 4 \int_{L_2} (S_+ - S_-) dE$ is determined to be -3.326 ± 0.380 .

c) Error estimation of NS_{emcd}

NS_{emcd} is estimated from experimental data as a ratio of $5 \int_{L_3} (S_+ - S_-) dE - 4 \int_{L_2} (S_+ - S_-) dE$ and $\int_{L_{2,3}} (S_+ + S_-) dE$. By using the integral values recorded above, our statistics for estimating the normalized strength of EMCD spectra (NS_{emcd}) provide values with good statistical significance. The error in NS_{emcd} can be estimated according to standard error propagation rules in the division process, as shown below:

$$X = \frac{u}{v}$$

$$\sigma_X^2 = \sigma_u^2 \left(\frac{\partial X}{\partial u} \right)_{\bar{u}}^2 + \sigma_v^2 \left(\frac{\partial X}{\partial v} \right)_{\bar{v}}^2$$

$$\sigma_X^2 = \frac{\sigma_u^2}{\bar{v}^2} + \frac{\sigma_v^2 \bar{u}^2}{\bar{v}^4}$$

Consequently, the error in NS_{emcd} ($S_{NS_{emcd}}$), the error in $5 \int_{L_3} (S_+ - S_-) dE - 4 \int_{L_2} (S_+ - S_-) dE$ ($5S$) and the error in $\int_{L_{2,3}} (S_+ + S_-) dE$ (S_{WL}) have the following relationship:

$$S_{NS_{emcd}} = \sqrt{\frac{(5S)^2}{\left(\int_{L_{2,3}} (S_+ + S_-) dE \right)^2} + \frac{S_{WL}^2 \left[5 \int_{L_3} (S_+ - S_-) dE - 4 \int_{L_2} (S_+ - S_-) dE \right]^2}{\int_{L_{2,3}} (S_+ + S_-) dE^4}}$$

As the error arising from independent measurements is uncorrelated, we obtained:

For Fe:

Inside the perfect domain: $S_{NS_{emcd}} = 0.036$; $NS_{emcd} = -0.263 \pm 0.036$;

Within the APB: $S_{NS_{emcd}} = 0.010$; $NS_{emcd} = -0.14 \pm 0.010$

For Ni:

Inside the perfect domain: $S_{NS_{emcd}} = 0.135$; $NS_{emcd} = -0.908 \pm 0.135$

Within the APB: $S_{NS_{emcd}} = 0.102$; $NS_{emcd} = -0.556 \pm 0.102$

The relative reductions in normalized EMCD strengths and their error bars are:

For Fe:

$$NS_{emcd_{relative}} = 1 - \frac{NS_{emcd_{APB}}}{NS_{emcd_{perfect}}} = 0.468 \pm 0.082 ,$$

meaning that there is a $\sim 46.8\% \pm 8.2\%$ reduction in the normalized strength of the Fe EMCD signal in the APB region, when compared to that in the perfect domains.

For Ni:

$$NS_{emcd_{relative}} = 1 - \frac{NS_{emcd_{APB}}}{NS_{emcd_{perfect}}} = 0.388 \pm 0.145$$

meaning that there is a $\sim 38.8\% \pm 14.5\%$ reduction in the normalized strength of the Ni EMCD signal in the APB region, when compared to that in the perfect domains.

Based on the error bars given above, the normalized strength of EMCD and the relative reduction in normalized EMCD strength are measured with good confidence levels. The error bar for Ni is naturally larger due to a lower SNR level in the raw Ni EMCD spectra.

DFT calculation details and J values of defect-free structure for different unit cell volumes

We first fully relaxed the lattice parameters and atomic positions of ordered NiFe_2O_4 in the $P4_122$ and $Imma$ structures. We found that the results are in good agreement with the experiment. By utilizing these relaxed lattice parameters, we constructed the APB structure models. Considering limited computational resources, we constructed a structure model with two APBs of sufficient mutual separation, in order to analyze the atomic positions and electronic structure properties. We fixed the lattice constants of the structure model and fully relaxed the internal atomic positions. We did not relax the volumes of the APB structures. We evaluated the J values of the bulk structure for different volumes and found that the differences were very small (see Table S3).

Magnetic coupling in the $Imma$ -APB $NiFe_2O_4$ structure by DFT calculations

In the perfectly-ordered $Imma$ $NiFe_2O_4$ structure, there are five symmetrically-independent magnetic exchange interactions between nearest neighbor magnetic ions that are connected *via* oxygen ions, namely: 90° - Fe_{oct} -O- Fe_{oct} , 90° - Fe_{oct} -O- Ni_{oct} , 90° - Ni_{oct} -O- Ni_{oct} , 120° - Fe_{tet} -O- Fe_{oct} and 120° - Fe_{tet} -O- Ni_{oct} , where Fe_{oct} and Ni_{oct} refer to Fe and Ni ions in octahedral interstices respectively, while Fe_{tet} denotes Fe ions in tetrahedral interstices (Figure S8 and Table S1). 90° interactions are formed between ions occupying octahedral sites, while 120° interactions are formed between ions in tetrahedral and octahedral sites. Interactions of the five magnetic pairs were calculated using the four-state method^[21]. Similarly, just as for the $P4_122$ structure, there is strong antiferromagnetic coupling in the case of 120° interactions, taking values of 0.0343 and 0.0223 eV for 120° - Fe_{tet} -O- Fe_{oct} and 120° - Fe_{tet} -O- Ni_{oct} , respectively. 90° interactions between octahedral sites are weaker than 120° interactions by an order of magnitude, having values of 0.0029, -0.0010 and -0.0012 eV for 90° - Fe_{oct} -O- Fe_{oct} , 90° - Fe_{oct} -O- Ni_{oct} and 90° - Ni_{oct} -O- Ni_{oct} , respectively. Antiferromagnetic interactions between Fe ions on octahedral sites in the $Imma$ ordered structure are stronger than in the $P4_122$ ordered structure. Magnetic structures (Figure S8b) for the $Imma - APB$ model, deduced from calculated exchange parameters (J), describe the most stable structure with the lowest energy compared with other alternative magnetic structures (see Figure S9).

Similarly, we analyzed the magnitudes of the magnetic moments and magnetic interactions for the $Imma - APB$ structure, which contains two APBs separated by 15 Å along the [110] direction (Figure S8). In contrast to $P4_122 - APB$, one of the inserted {111} layers consists completely of Fe ions, while the other inserted {111} layer contains alternately-stacked Fe and Ni atomic columns in the [011] direction.

First-principles density functional theory (DFT) calculations indicate that the Ni ions in the inserted {111} layers are different from those in the perfectly-ordered structure. A statistical analysis of the distribution of the magnitudes of magnetic moments is shown in Figure S8c. The results show that the local magnetic moments of the Ni ions decrease by almost 50% due to their change to low-spin state Ni^{4+} (d^6) ions. The results of the calculations are consistent with the decreased Ni signal in the EMCD experiment. In contrast, the magnitude of the magnetic moments of the Fe ions stays almost unchanged in the APB, when compared to that in the perfect domains (Figures S8b and S9a), but the coupling between the Fe atoms in the interlayer with the rock salt structure tends to be antiferromagnetic. Two types of 90° magnetic interactions in the APB region were considered. Antiferromagnetic coupling of 90° - $\text{Fe}_{\text{oct}}\text{-O-Fe}_{\text{oct}}$ was found to be enhanced, whereas strong antiferromagnetic coupling was found for 90° - $\text{Fe}_{\text{oct}}\text{-O-Fe}_{\text{oct}}$, in contrast to weak antiferromagnetic coupling found in the perfectly-ordered *Imma* structure. In the areas of perfect domains closest to the APB, 90° magnetic couplings exhibit an enhanced interaction compared to that in the perfectly-ordered domain. As a result of the decrease in the magnetic moment of Ni inside the APB, the 120° - $\text{Fe}_{\text{tet}}\text{-O-Ni}_{\text{oct}}$ interaction strength decreases significantly. However, the 120° - $\text{Fe}_{\text{tet}}\text{-O-Fe}_{\text{oct}}$ interaction is enhanced to 0.0468 eV, which can be compared with a value of 0.0343 eV in the perfect domain. In contrast to the situation in the $P4_122$ – APB structure, the insertion of a defected rock salt structure in {111} layers leads to the introduction of 170° - $\text{Fe}_{\text{oct}}\text{-O-Ni}_{\text{oct}}$. DFT calculations also suggest rather strong antiferromagnetic coupling for the 170° magnetic coupling (0.0277 eV), which results in antiferromagnetic coupling between Fe ions in the inserted {111} planes. This behavior also explains the significant decrease in the Fe signal detected in the EMCD experiment.

References

- [39] a) J. Barthel, J. Mayer, J. Ruzs, P. L. Ho, X. Y. Zhong, M. Lentzen, R. E. Dunin-Borkowski, K. W. Urban, H. G. Brown, S. D. Findlay, L. J. Allen, *Phys. Rev. B* **2018**, *97*, 144103; b) M. C. Richter, J. M. Mariot, O. Heckmann, L. Kjeldgaard, B. S. Mun, C. S. Fadley, U. Lüders, J. F. Bobo, P. De Padova, A. Taleb-Ibrahimi, K. Hricovini, *Eur. Phys. J. Special Topics* **2009**, *169*, 175.
- [40] a) O. Šipr, J. Vackář, J. Minár, *J. Synchrotron Rad.* **2018**, *25*, 523; b) K. Carva, D. Legut, P. M. Oppeneer, *Europhys. Lett.* **2009**, *86*, 57002; c) K. Carva, M. Battiato, D. Legut, P. M. Oppeneer, *Phys. Rev. B* **2013**, *87*, 184425.
- [41] A. Rose, *The Quarterly Review of Biology* **1975**, *50*, 506.
- [42] a) J. Ruzs, S. Rubino, P. Schattschneider, *Phys. Rev. B* **2007**, *75*, 214425; b) L. Calmels, F. Houdellier, B. Warot-Fonrose, C. Gatel, M. J. Hÿtch, V. Serin, E. Snoeck, P. Schattschneider, *Phys. Rev. B* **2007**, *76*, 060409.